Si Solution in θ-Al$_{13}$Fe$_4$ from First-Principles

C. M. Fang[1*], Z. P. Que[1], A. Dinsdale[2, 1] and Z. Fan[1]

[1]BCAST, Brunel University London, Kingston Lane, Uxbridge, Middlesex, UB8 3PH, UK.

[2]Hampton Thermodynamics Limited, UK.

Corresponding author: Changming Fang,

e-mail: changming.fang@brunel.ac.uk

Highlights

- Si prefer on the Al8 and Al9 sites, forming $\theta\text{-Al}_{70}(Si,Al)^{IX}_4(Al,Si)^{VIII}_4Fe_{24}$;
- Lattice parameters and volume of the unit cell decrease linearly with Si content;
- The calculated results agree with the experimental data in the literature;
- $\theta\text{-(Al, Si)}_{13}Fe_4$ exhibits ionic, covalent and metallic triple nature.

Abstract

θ-Al$_{13}$Fe$_4$ forms as a primary Fe-intermetallic compound (Fe-IMC) in the casting processes of most Al alloys. Si is added to Al alloys to improve the mechanical performances of the products. Fe-IMCs including (Si doped) θ-Al$_{13}$Fe$_4$ have nontrivial impacts on the mechanical performances of the solidified Al-based parts. Here, we investigate systematically Si solution in θ-Al$_{13}$Fe$_4$ using *ab initio* density functional theory (DFT). We reveal that Si prefer substitution on two Al sites (Al9 and Al8) in θ-Al$_{13}$Fe$_4$, forming θ-Al$_{70}$(Si,Al)$^{IX}_4$(Al,Si)$^{VIII}_4$Fe$_{24}$ (the Roman numerals represent the Al sites [13]). The calculations identify a linear relation between the lattice parameters of the unit cell and the Si content. The knowledge obtained here is useful to get insight into the formation and structural and chemical properties of the Fe-Al-Si intermetallic compounds and to optimize the microstructures and properties of the solidified Al based alloys.

Key words: Fe-intermetallic compounds; Silicon substitution; *Ab-initio* calculations; Structural properties; θ-Al$_{13}$Fe$_4$

1. Introduction

Iron and silicon exist as impurities in most aluminium alloys. Due to the small solubility in Al, Fe remain in the form of Fe-containing intermetallic compounds (Fe-IMCs) which deteriorate the mechanical performances of Al-based components [1-3]. Moreover, Si is widely added into Al alloys to improve the mechanical performances of the products [1, 2]. The recycling economy requires that harmful Fe-IMCs including θ-Al$_{13}$Fe$_4$ are minimized or at least controlled in the products during the casting processes of Al alloys, especially Al scraps which contains variable amounts of Fe and Si [4, 5]. To reach this goal, knowledge about Si solubility in the Fe-IMCs, including θ-Al$_{13}$Fe$_4$ is a pre-requisite.

θ-Al$_{13}$Fe$_4$ is the phase richest in Al in the Fe-Al binary system [6-8]. Experiments showed that θ-Al$_{13}$Fe$_4$ contains Si and occurs most frequently in competition with other Fe-IMCs in cast Al-based alloys [9-12]. Moreover, the primary θ-Al$_{13}$Fe$_4$ phase may transform into other Fe-IMC phases, e.g. hexagonal α-Al$_8$Fe$_2$Si or monoclinic/orthorhombic β-Al$_5$FeSi during thermal treatments of Al alloys [9-12]. Structurally, θ-Al$_{13}$Fe$_4$ has a rich variety of crystal chemistry. It has a monoclinic lattice with space group C2/m (nr. 12) [13]. There are 20 crystallographically different atomic species (5 Fe and 15 Al) and 102 atoms in total in a unit cell (Fig. 1 and Table S-I). The Al atoms have 10 to 12 metal neighbours including 2 to 4 Fe neighbours, except the Al2 atoms at the Wyckoff 4i sites which have only 6 neighbours including two Fe with Fe-Al bond-lengths below 3.0 Å (1 Å = 0.1 nm = 10^{-10} m). The Fe atoms have coordination numbers ranging from 9 to 11 with Fe-Al bond-lengths below 3.0 Å.
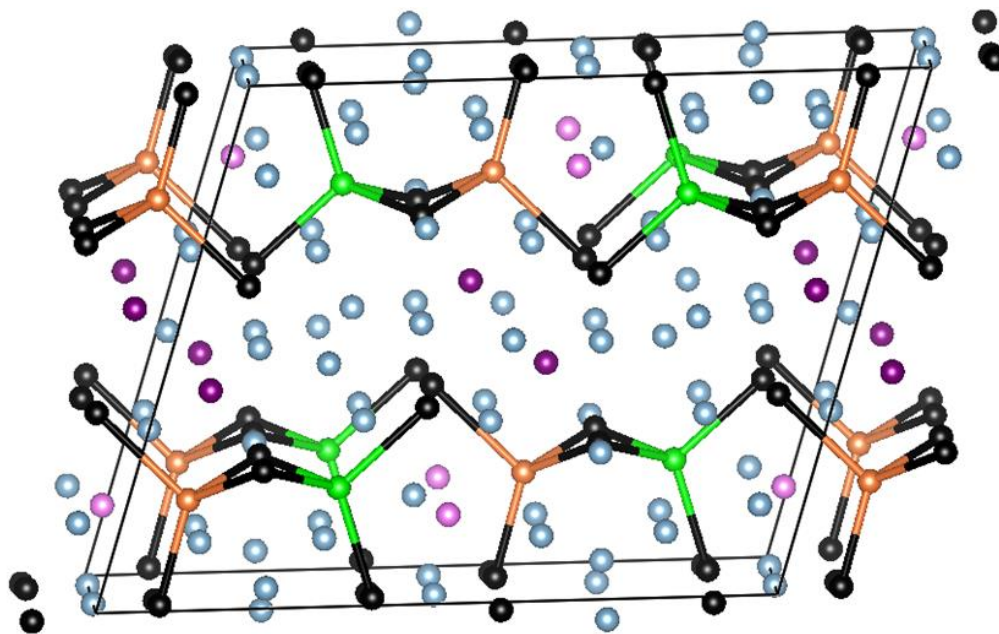

Fig. 1. (Colour online) Schematic structure of θ-Al$_{13}$Fe$_4$ approximately along its [0 1 0] axis. The parallel axis is the *a*-axis and the vertical axis is the *c*-axis. The black spheres represent the Fe atoms. All the other spheres represent Al: the green spheres represent Al8, the orange spheres Al9 sites, the violet Al4 and the light pink Al6 and the silvery for the rest Al atoms according to the Grin's assignments [13]. The bonds between Al8 and Al9 with Fe atoms are also displayed.

Various experimental studies were conducted on Si solution in θ-Al$_{13}$Fe$_4$ [1-3, 9-12, 14-17]. Casting experiments revealed a rich variety of Si containing Fe-IMCs, including θ-Al$_{13}$Fe$_4$ in the final alloys, depending on the chemical compositions of the alloys and the casting conditions [1-3, 15-17]. As shown in the critically assessed Al-Fe-Si ternary phase diagram, there appears to be limited Si solubility in θ-Al$_{13}$Fe$_4$ at elevated temperatures [14-17]. Stefaniary, Grieger and Turmezey reported

complex relations between the lattice parameters of the unit cell and the Si and Fe compositions in θ-$Al_{13}Fe_4$ [18]. There is still however, insufficient information about the chemical composition of Si solution in this phase and their relative stability to other Fe-IMCs. This is partially due to the experimental difficulties to obtain samples of high purity.

Theoretical approaches, especially parameter-free first-principles methods can be useful in this aspect. First-principles density-functional approaches have been applied to investigate the structural, electronic and magnetic properties of pure θ-$Al_{13}Fe_4$ [19-22], its surfaces for catalysis [23, 24], as well as the intrinsic defects in this binary compound [25, 26]. However, till now Si solubility in most Fe-IMs, including θ-$Al_{13}Fe_4$ is largely unknown. In this paper, we present the results of a first-principles density-functional theory (DFT) study on the formation, stability and structural and electronic properties of Si solution in θ-$Al_{13}Fe_4$, the Al richest compound in the Al-Fe system. The calculations identify the favoured sites for substituting Si in θ-$Al_{13}Fe_4$. The study also identifies a relationship between the lattice parameters of the unit cell and Si content in θ-$Al_{13}Fe_4$. The obtained information here sheds some light on Si solubility in θ-$Al_{13}Fe_4$ and is helpful to get insight into Si solution in other Fe-IMCs.

2. Methods

The first-principles' Vienna *Ab initio* Simulation Package (VASP) [27, 28] was employed for the present calculations. This code employs the Density-Functional Theory (DFT) within the Projector-Augmented Wave (PAW) approach [29, 30]. The spin-polarized Generalized Gradient Approximation (GGA-PBE) [30, 31] was applied for the exchange and correlation energy terms because the GGA approximations describe the 3d metals such as iron and related compounds better than the Local Density Approximation (LDA) [25, 31, 32]. The cut-off energy of the wave functions was set to 550 eV and the cut-off energy of the augmentation functions to 700 eV (1eV is equal to $1.6022×10^{-19}$ J). These values are higher than the corresponding default values (*Enmax/Eaug* = 240.3 eV/291.1 eV for Al, 267.9 eV/511.4 eV for Fe and 245.3 eV/322.1 eV for Si, respectively). The electronic wave functions were sampled with a dense, e.g. a 4×8×6 grid (70 to 100 *k*-points) in the irreducible Brillouin zone (BZ) of θ-$Al_{13}Fe_4$ and the related compositions depending on the symmetry, using the Monkhorst–Pack method [33]. First-principles structural optimizations were performed for both lattice parameters and the coordinates of the atoms. Different *k*-meshes and cut-off energies were used for the wave functions and augmentation wave functions, respectively. Tests showed good convergence (<1 meV per atom).

The formation energy of a doped foreign element (Fe or Si) into α-Al is defined as [25, 32]:

$$\Delta E_{im}(Al_nM) = E(Al_nM\} - [n\,E(Al) + E(M)] \tag{1}$$

Here $E(M)/E(Al)$ is the total valence electron energy of the solid element M/Al, $E(Al_nM\}$is the energy for the doped system Al_nM, respectively. The calculated formation energy $\Delta E_{im}(Al_nM)$ represents the energy cost to dope an impurity M in Al with respect to their elemental solids. A $3a_0×3a_0×3a_0$ (a_0 is the lattice parameter of the conventional cell of α-Al) supercell which contains 108 atoms was employed for the impurity calculations. The unit of the formation energy is eV per doped atom.

The formation energies of the Al-Fe binary compounds with respect to the elemental solids, Al and Fe is defined as [25, 32]:

$$\Delta E_{form}(Al_mFe_n) = \{E(Al_mFe_n\} - [mE(Al) + nE(Fe)]\}/(n+m) \tag{2}$$

The unit for the formation energies of the binary compounds is eV/atom (1 eV/atom = 96.45 kJ/mol).

Furthermore, to have a measure of the relative stability of Si doped $Al_{13}Fe_4$ with respect to the parent intermetallic compound and the elemental solids (α-Al, α-Fe and diamond-Si), the formation energy per

cell for Si doping in the compounds is given by:

$$\Delta E_{Si}(Al_{13}(Fe_{1-x}Si_x)_4) = E\{Al_{13}(Fe_{1-x}Si_x)_4\} - \{E(Al_{13}Fe_4) + 4x[E(Si) - E(Fe)]\} \qquad (3a)$$

$$\Delta E_{Si}((Al_{1-x}Si_x)_{13}Fe_4) = E\{(Al_{1-x}Si_x)_{13}Fe_4\} - \{E(Al_{13}Fe_4) + 13x[E(Si) - E(Al)]\} \qquad (3b)$$

The unit of the formation energy is eV/f.u., here f.u. represents "formula unit".

At the temperature $T = 0$ K and the pressure $p = 0$ Pa, the enthalpy difference is equal to the energy difference, $\Delta H = \Delta E$, when the zero-point vibration contribution is not taken into account. A negative value of the formation energy means that the formation is exothermic and that this reaction is favoured.

3. Results and discussion

We firstly report the results of the structural optimizations for the elemental solids, α-Al, α-Fe and Si [34, 35], the dilute solutions of Fe and Si in solid Al and for stoichiometric θ-Al$_{13}$Fe$_4$ (Fig. 1). The results are listed in Table I with a comparison with the selected experimental data in the literature. The calculated atomic coordinates for the binary compound are listed in Table S-I together with selected experimental data in the literature. As shown in Table I, the calculated lattice parameters for the elemental solids are in good agreement with the experimental values with the corresponding differences within 1%.

Table I shows that iron prefers to be doped in Al with a formation energy (ΔE_{im}) of -0.457 eV/Fe with respect to the elemental solids, whereas Si doping in solid Al is not favoured with a formation energy as high as +0.431 eV/Si in Al at 0 K. For the binary θ-Al$_{13}$Fe$_4$ compound the calculations reproduced well the experimental lattice parameters in the literature (differences within 1 %). The calculated formation energy for θ-Al$_{13}$Fe$_4$ is slightly more negative than the experimental values which do have appreciable scatter as shown in Table I [6, 7, 25, 36].

Table I. Calculated results (lattice parameters, formation energies and magnetic properties) of the related elemental solids (α-Al, α-Fe and Si), the dilute solutions of Fe and Si in α-Al and the pure θ-Al$_{13}$Fe$_4$ phase at 0 K using the DFT-PBE method. Experimental values in the literature (for the elemental solids at 0 K) [34] and for the binary compound at room temperature were included in the parenthesis for comparison. The formation energies, ΔE are based on the total energy calculations and equations 1 and 2 for the impurity and the compound, respectively. $\Delta = (d_{exp} - d_{calc})/d_{exp}*100$ (%) measures the deviation of the calculated lattice parameters from the experimental ones. FM represents ferromagnetic, NM non-magnetic.

Elements	Lattice/space group	Lattice parameters(Å) /Δ	M(μ$_B$/M)	ΔE_{im}
α-Al	FCC/Fm-3m (225)	4.039 (4.0325) [34] / -0.2 %		-
α-Fe	BCC/Im-3m (229)	2.831 (2.8607) [34] / -1.0 %	2.18 (2.10)&	-
Si	FCC/Fd-3m(227)	5.468 (5.42982) [34] /+0.7 %		-
Solutes		Bond lengths (Å)		
Fe* in Al	-	Fe-Al: 2.74(×12)	NM	-0.457 eV/Fe
Si* in Al	-	Si-Al: 2.84(×12)	-	+0.431 eV/Si
Binary	Space group	Lattice parameters(Å) /Δ		ΔE_{form}
θ-Al$_{13}$Fe$_4$	Mon./C2/m (12)	$a = 15.426$ (15.492 [13]) /-0.4 % $b = 8.022$ (8.078 [13]) /-0.7 % $c = 12.425$ (12.471 [13]) /-0.3 % $\beta = 107.68°$ (107.69 [13]) /0.0 %	NM	-0.330 eV/atom (-0.225 to -0.310 eV/atom) [6,7,25,36]

Grin and co-workers performed a refinement of the crystal structure of θ-Al$_{13}$Fe$_4$ based on single-crystal diffraction data [13]. As shown in Table S-I, θ-Al$_{13}$Fe$_4$ has 20 crystallographically different atomic species, which assignments are used in present paper. In the calculations, we firstly replace one

atom at each Al site and at each Fe site by a Si atom, respectively. The formation energies were obtained from the calculations via equation 3.

The calculations showed that replacement of one Fe atom by Si in θ-Al$_{13}$Fe$_4$ costs between 2.01 eV and 2.57 eV with respect to the elemental solids and θ-Al$_{13}$Fe$_4$. As shown in Table I, dilute solution of Fe in solid Al is favoured. Therefore, the costs of Si incorporation in the Fe sites become even high if we take the formation energy of dilute Fe solution in α-Al as reference. Such high costs indicate that Si doping on the Fe sites is very unlikely.

Here we address the results of Si incorporation in the 15 inequivalent Al sites. The detailed results for one Si doping on the Al sites are listed in Table II.

Table II. Calculated results (lattice parameters, bonds and doping energies at 0 K) for one Si doping on each of the 15 inequivalent Al sites in θ-Al$_{13}$Fe$_4$ using the first-principles DFT-GGA-PBE approach.

	Lattice parameters (Å) a b c $\beta(°)$	Si-Al/Fe (Å)	ΔE_{Si} (eV/cell)
Pure	15.426, 8.022, 12.425, 107.68	-	0.0
Si at Al1(4i)	15.409, 8.034, 12.394, 107.71	Si-Fe: 2.36, 2.43, 2.51 Si-Al:2.48, 2.82×2,2.85×2,2.87×2	+0.149
Si at Al2(4i)	15.419, 8.010, 12.442, 107.70	Si-Fe: 2.16×2 Si-Al: 2.93×2,2.97×2,3.05×2, 3.07×2,3.21×2	+0.313
Si at Al3(4i)	15.391, 8.028, 12.431, 107.82	Si-Fe: 2.32, 2.37 Si-Al: 2.70×2,2.76×2,2.84, 2.85×2,2.86×2,2.96×2	+0.454
Si at Al4(4i)	15.406, 8.023, 12.410, 107.62	Si-Fe: 2.42, 2.52×2, 2.54 Si-Al, 2.50,2.51,2.63×2, 2.74,2.74×2	+0.040
Si at Al5(4i)	15.363, 8.032, 12.437, 107.58	Si-Fe: 2.27,2.28 Si-Al: 2.74,2.74×2, 2.78×2,2.85×2, 2.89×2,2.91	+0.323
Si at Al6(4i)	15.411, 8.029, 12.397, 107.72	Si-Fe: 2.37, 2.40, 2.45 Si-Al: 2.51, 2.82×2,2.84×2,2.88×2	+0.020
Si at Al7(2d)	15.394, 8.023, 12.405, 107.46	Si-Fe: 2.37×2 Si-Al: 2.67, 2.67×2, 2.79×2, 2.79×2,3.22×2	+0.207
Si at Al8(4i)	15.416, 8.012, 12.409, 107.66	Si-Fe: 2.40 ×2, 2.50 Si-Al: 2.52, 2.62, 2.65×2, 2.66×2, 2.81×2	-0.014
Si at Al9(4i)	15.413, 8.015, 12.405, 107.64	Si-Fe: 2.37, 240×2, 2.82 Si-Al: 2.52×2, 2.61×2,2.66,2.67×2	-0.077
Si at Al10(8j)	15.416, 8.021, 12.413, 107.78	Si-Fe: 2.41, 2.46, 2.58 Si-Al: 2,61, 2.63, 2.74, 2.76, 2.82, 2.84,2.86, 2.89, 3.14	+0.226
Si at Al11(8j)	15.417, 8.024, 12.403, 107.61	Si-Fe: 2.39, 2.43 Si-Al: 2.58, 2.61, 2.65, 2.76, 2.78, 2.82, 2.84, 2.85×2, 3.05	+0.218
Si at Al12(8j)	15.398, 8.024, 12.417, 107.52	Si-Fe: 2.38, 2.48. 2.56 Si-Al: 2.58, 2.62, 2.79, 2.84, 2.86×2, 2.88, 3.02, 3.16	+0.223

Si at Al13(8j)	15.394, 8.024, 12.428, 107.77	Si-Fe: 2.36, 2.42, 2.51 Si-Al: 2.64, 2.69, 2.72, 2.79, 2.84, 2.86, 2.89, 3.13, 3.19	+0.184
Si at Al14(8j)	15.406, 8.023, 12.410, 107.62	Si-Fe: 2.42, 2.52×2, 2.54 Si-Al: 2.50, 2.51, 2.63×2,2.74,2.74×2.	+0.101
Si at Al15 (4g)	15.405, 8.014, 12.429, 107.64	Si-Fe: 2.40 ×2, 2.240×2 Si-Al: 2.78×2, 2.78×2, 2.86×2, 2.90×2	+0.114

It is notable that partial replacements at the Al sites by Si break the local symmetry, and correspondingly change the lattice symmetry of the crystal from being monoclinic to being triclinic. However, the calculations showed that the deviation of the Si doped crystals from the pure phase is minor and the doped system can be treated as monoclinic (pseudo).

Table II shows that Si doping is favoured at both the Al9 and Al8 sites. Moreover, the energy cost of Si doping at the Al6 and Al4 is minor (+0.020 eV and +0.040 eV, respectively). The four Al species are at the Wyckoff 4i sites with a mirror symmetry (m), and each Al at these sites has three or four Fe neighbours. As shown in Table II, each atom at the Al2, Al3 and Al5 sites has only two Fe neighbours and Si incorporation in these sites costs energies higher than 0.3 eV. This indicates Si prefers sites with more than two Fe neighbours. This conclusion is also true for Si incorporation in the Al7 sites (ΔE_{Si} = 0.207 eV) as shown in Table II.

Meanwhile, as shown in Table II Si doping is not favoured on the remaining Al sites, including the 8j sites with doping energies >0.100 eV/Si. The 8(j) sites have the site symmetry C_1. This indicates local symmetry and multiplicity of the Al sites may play a role in Si incorporation.

We also investigated higher compositions of Si doping on the Al sites in a systematic way. The formation energies for various Si contents for the more stable configurations are plotted in Fig. 2 with details in Table S-II. The calculations showed that the most stable configurations have Si at the Al9 sites. The formation energy decreases with increasing Si content and reaches a minimum at x(Si) = 0.051, which corresponds to fully occupying the Al9 sites by Si with chemical formula $Al_{74}Si^{IX}_4Fe_{24}$, where the Roman numeral represents the Al site. Then the formation energy increases with increasing Si content. As shown in Fig. 2, the maximum Si doping is reached with x(Si) = 0.103, corresponding to the full occupation of both Al9 and Al8 sites by Si which has the chemical formula $Al_{70}Si^{IX}_4Si^{VIII}_4Fe_{24}$. Beyond this composition, the formation energy becomes positive. The formation energy is +0.163 eV/unit cell for x(Si) = 0.115. The study also revealed extra freedom of Si occupation, which has impact on the free energy of the system at elevated temperature. This will be addressed later.
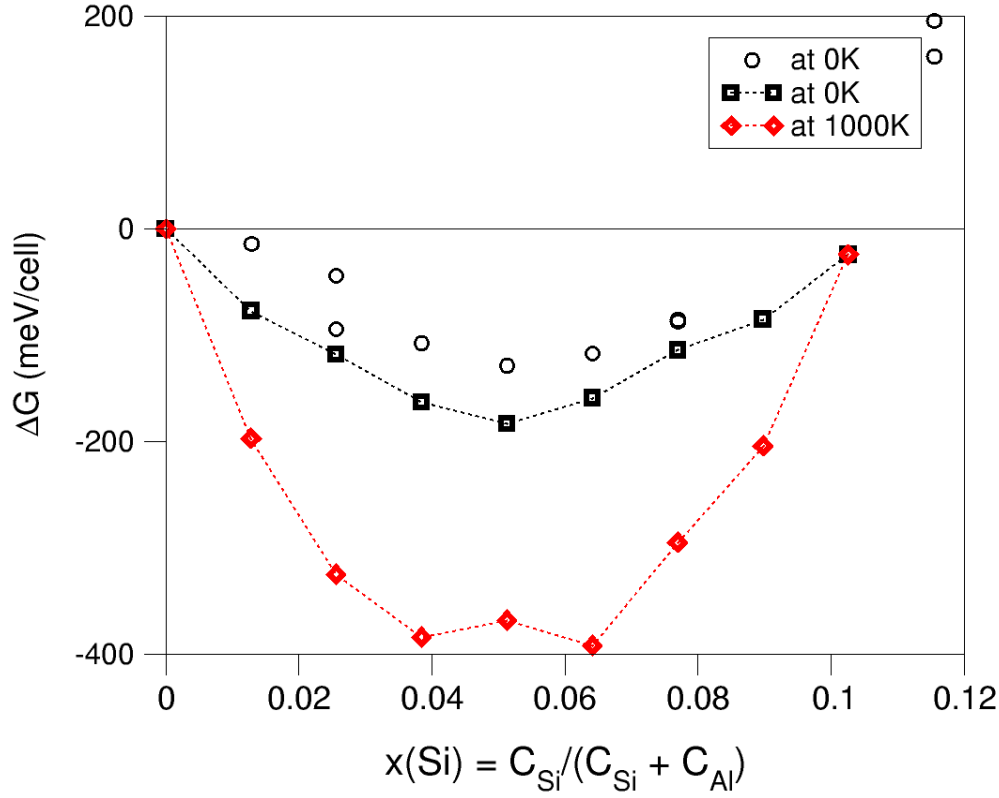
Fig. 2. (Colour online) The dependence of the formation free energies on the composition of Si doped in θ-(Al$_{1-x}$Si$_x$)$_{13}$Fe$_4$ at 0 K for configurations of high stability and at 1000 K for the most stable configurations at different Si contents. The spheres represent the formation energies at 0 K for the more stable configurations. The dotted-line linked squares represent the most stable configurations with Si occupying series at the Al9 firstly and then the Al8 sites. C$_{Si}$ and C$_{Al}$ represent the Si and the Al components in θ-(Al$_{1-x}$Si$_x$)$_{13}$Fe$_4$, respectively.

Next, we address the relationships between the lattice parameters of the unit cell and the Si content. The calculated values for the more stable configurations are plotted in Fig. 3. The calculations showed little variation of the angle β for the configurations of different Si content. There is a simple linear decrease of the lattice parameters and the unit cell volume with increasing Si content (Fig. 3).

Experimentally, Stefániay and co-workers investigated the dependences of the lattice parameters and the unit cell on the compositions of Fe and Si impurities [18]. They reported complex relations: with increasing Si content, the length of the *a*-axis decreases, whereas the length of the *b*-axis and the volume of the unit cell increase. This observed behaviour is not in line with our first-principles calculations. We consider that their results are not comparable with the calculations due to the difficulties in experiments to accurately measure the Si and Fe compositions in the samples.

Recently Que and colleagues obtained small single crystals from the cast Al alloys [3]. The author also selected crystals containing different Si content from the cast Al alloys [37]. Structure refinements on the X-ray diffraction patterns for the single crystals revealed the lattice parameters: $a = 15.447$ Å, $b = 8.057$ Å, $c = 12.429$ Å and $β = 107.80$ ° for a single crystal without Si, θ-Al$_{13}$Fe$_4$; and $a = 15.424$ Å, $b = 8.052$ Å, $c = 12.404$ Å and $β = 107.65$ ° for a single crystal with Si, θ-(Al$_{1-x}$Si$_x$)$_{13}$Fe$_4$ with $x = 0.026$ [37]. Clearly, the lattice parameters of the pure θ-Al$_{13}$Fe$_4$ are slightly larger than the corresponding values of θ-(Al$_{0.974}$Si$_{0.026}$)$_{13}$Fe$_4$. This experimental results are in line with the first-principles calculations.
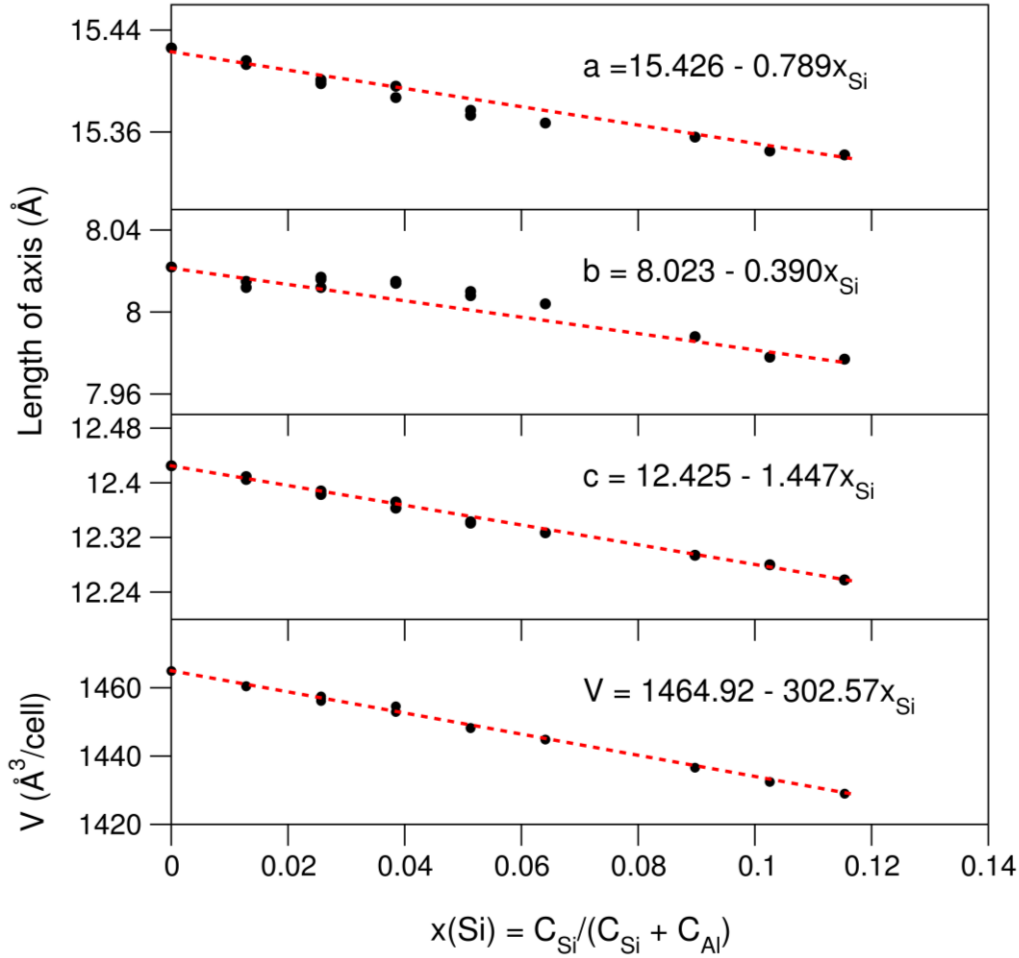
Fig. 3. (Colour online) Dependence of the axis lengths and the volume of θ-$(Al_{1-x}Si_x)_{13}Fe_4$ phase on the Si content at ambient temperature. C_{Si} and C_{Al} represent the Si and the Al components in θ-$(Al_{1-x}Si_x)_{13}Fe_4$, respectively.

To get some insight into the chemical bonding in the θ-phase, we analysis the local chemical bonding between Si and the neighbouring Fe atoms for θ-$Al_{74}Si^{IX}_4Fe_{24}$, the crystal with the lowest formation energy and θ-$Al_{70} Si^{IX}_4Si^{VIII}_4Fe_{24}$, the configuration with the highest Si content,. The symmetry of the two crystals keeps same as the pure θ-$Al_{13}Fe_4$. The important interatomic distances between Si(Al) and the Fe atoms are listed in Table III. We also performed electronic structure calculations for these crystals. The iso-surfaces of the valence-electron density distributions of the two crystals are shown in Fig. 4. Curves of the partial density of states (pDOS) of the selected atoms and the total density of states of $(Al_{1-x}Si_x)_{13}Fe_4$ with $x = 0.051$ and $x = 0.103$ are shown in Fig. 5.

The Si-Fe interatomic distances are slightly shorter than the corresponding Al-Fe bond-lengths as shown in Table III. This agrees with the results that the lattice parameters of the unit cell decrease with increasing Si content in the $(Al_{1-x}Si_x)_{13}Fe_4$ crystals, as shown in Fig. 3.

Table III. Interatomic distances between Si/Al atoms at the Al9/Al8 sites and the Fe atoms, the Bader charges at the (Al,Si)9 and (Al,Si)8 sites in pure θ-$Al_{13}Fe_4$ and the Si doped crystals at ambient conditions.

Compounds	Al(Si)-Fe bond-length (Å)	Charge (e/atom)
θ-$Al_{13}Fe_4$	Al9-Fe3: 2.46, -Fe5: 2.49($\times$2)	Al9: +1.09
	Al8-Fe4: 2.61, -Fe5: 2.47($\times$2)	Al8: +1.28
θ-$(Al_{0.9487}Si_{0.0513})_{13}Fe_4$	Si9-Fe3: 2.37, -Fe5: 2.41($\times$2)	Si9: -1.16

	Al8-Fe4: 2.59, -Fe5: 2.48(×2)	Al8: +1.29
θ-(Al$_{0.8974}$Si$_{0.1026}$)$_{13}$Fe$_4$	Si9-Fe3: 2.36, -Fe5: 2.43(×2)	Si9: -1.25
	Al8-Fe4: 2.42, -Fe5: 2.47(×2)	Si8: -0.89

Both Fe and Si atoms are surrounded by dense electron clouds (Fig. 4). This corresponds well to the itinerant Fe 3d states and the semi-localized Si 3s states, respectively. In Al$_{74}$Si$^{IX}_4$Fe$_{24}$ there are Si-Fe clusters. Each Si atom is coordinated to three Fe atoms. There are Fe-Si linked networks in Al$_{70}$Si$^{IX}_4$Si$^{VIII}_4$Fe$_{24}$ (Fig. 4). The iso-surfaces of valence-electron density between the Si and Fe atoms indicates strong Si-Fe chemical bonding. In both crystals, there are no notable electron clouds around the Al atoms, in agreement with its free electron nature.

The curves of the partial density of states (pDOS) of Al8 atoms/ions in Al$_{74}$Si$^{IX}_4$Fe$_{24}$ provide us the general behaviours of the Al 3s and 3p eigen states in the intermetallic compounds. Both Al 3s and 3p states are distributed across the whole valence and conduction bands, reflecting its free-electron nature in the metallic compound. On the other hand, the pDOS curves of Si 3s and 3p states exhibit different behaviour. The Si 3s states dominate the lower part of the valence band between -11.6 eV to -10.0 eV. There is an isolated peak in the Si 3s density of states at about -11.0 eV for the Si atoms in the two crystals. This corresponds to the semi-core nature of the orbit. Interestingly, there are notably differences in the heights of the bonding Si 3s peaks corresponding to the Si9 atoms in Al$_{74}$Si$^{IX}_4$Fe$_{24}$ and the Si9 and Si8 atoms in the Al$_{70}$Si$^{IX}_4$Si$^{VIII}_4$Fe$_{24}$ crystals. This means that the semi-core Si 3s states also have chemical interaction with the neighbouring atoms. These differences of the local chemical bonding with the neighbouring atoms including the Fe atoms are shown in Table III. The antibonding Si 3s and 4p states hybridized with Al 3s, 3p and Fe 4s 4p states across all the valence and the conduction bands.
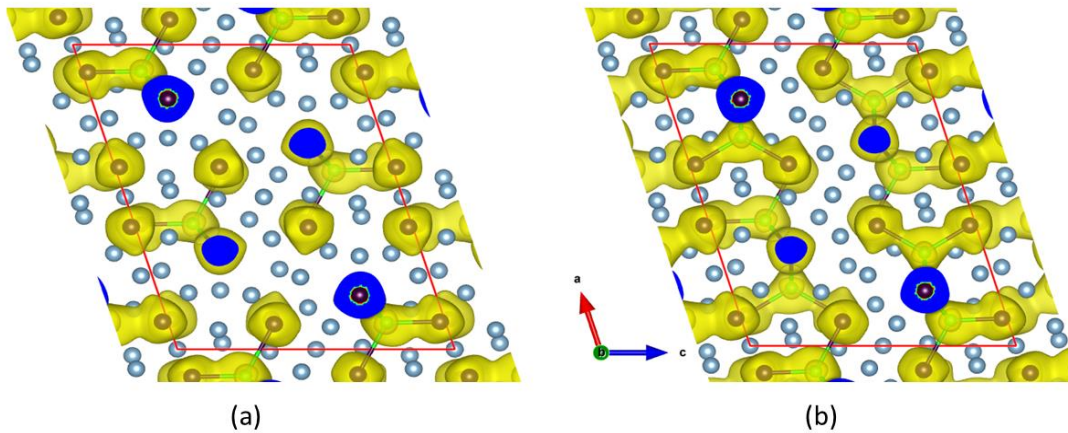

(a)   (b)

Fig. 4. (Colour online) The atomic arrangements and iso-surfaces of the valence-electron density distribution ($\rho_0(r) = 0.05$ e/Å^3) for Al$_{74}$Si$^{IX}_4$Fe$_{24}$ (a) and Al$_{70}$Si$^{IX}_4$Si$^{VIII}_4$Fe$_{24}$ (b) crystals at 0 K. The yellow clouds represent the iso-surfaces. The silvery spheres represent Al, the dark spheres Fe and the green Si.
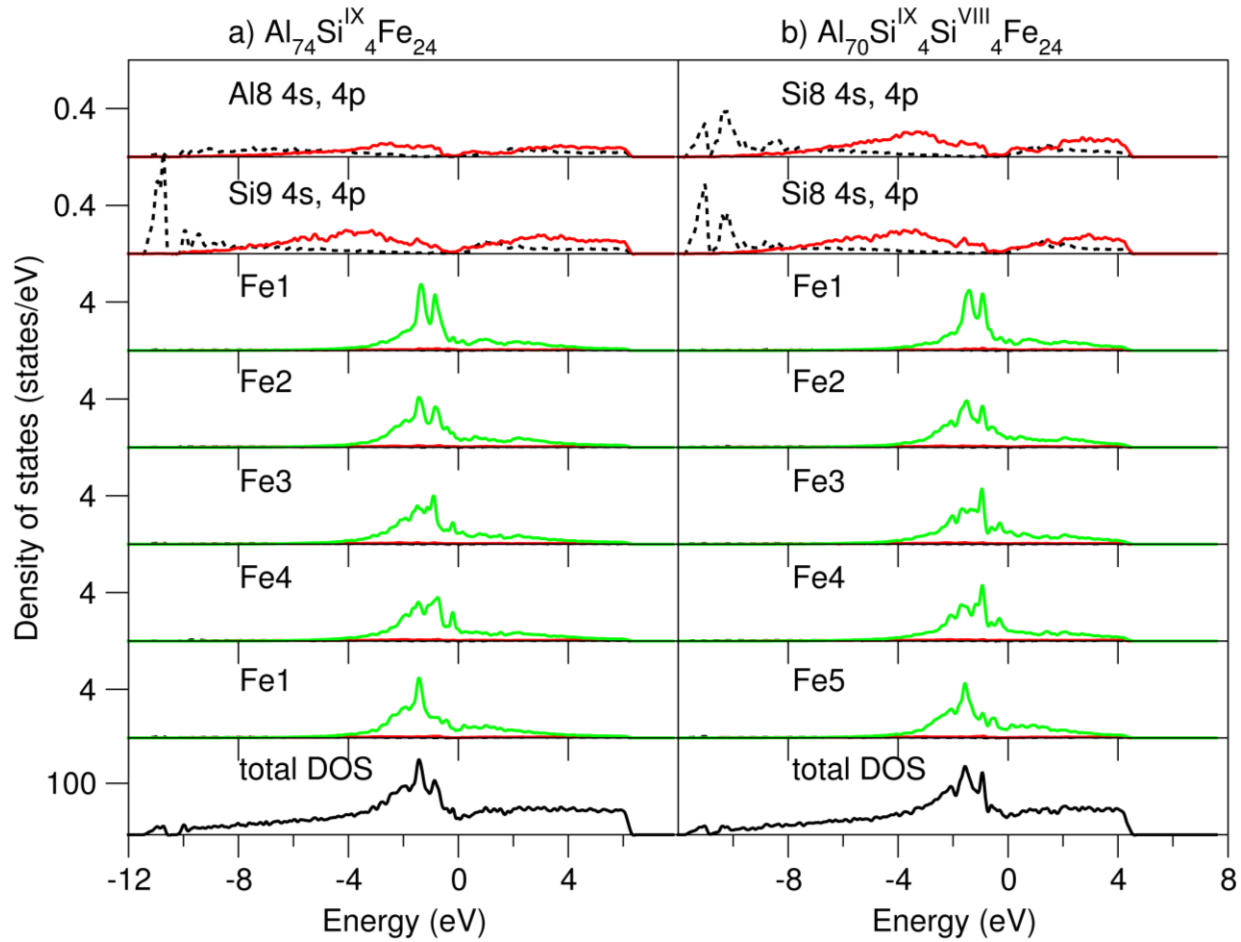
Fig. 5. (Colour online) Total and partial density of states near the Fermi level (at zero eV) for the two Si doped compositions at 0K. The dotted lines represent Al/Si 3s and Fe 4s, the red liens Al/Si 3p, Fe 4p and the green lines Fe 3d states, the filled black lines represent the total density of states of the unit cells.

The partial DOS curves of the Fe atoms/ions in the crystals show dual characteristics. The Fe 3d states exhibit itinerant nature and occur mainly within the energy range between -4.0 eV to 0.0 eV with some tails above the Fermi level, whereas the Fe 4s and 4p states are hybridized with Al/Si 3s and 3p states, being delocalized overall the whole valence and conduction bands. The Fe 3d states are almost fully occupied. The density of Fe states at the Fermi level is low (<0.8 states/eV). This indicates the stability of the non-spin-polarization solution [38]. The almost fully occupation of the Fe 3d states means that the Fe atoms have excess electrons. The different shapes of the curves of the density of the 3d states of the different Fe species come from the local crystal-field splitting.

The Bader charge analysis model provided a unique approach to define the shape and volume of an atom in solid [39]. The Bader change method is implemented within the VASP code [40]. We applied this method to get the Bader charges at the atomic sites of the studied crystals using the optimized valence-electron density distributions from the first-principles electronic structure calculations. The important results are included in Table III. The analysis also showed that the charges at the related Fe sites change but slight (about 0.2 e/Fe) after Si doping at the Al sites. This indicates dominantly covalent bonding between Fe and Si. As shown in Table III, clearly the Al atoms lost electrons to the Si atoms and Fe atoms. This corresponds to the values of the elemental electronegativity (1.61 for Al vs. 1.90 for Si and 1.83 for Fe, in Pauling scale).

The analysis shows that Si doped θ-Al$_{13}$Fe$_4$ crystals exhibit ionic, covalent and metallic triple nature. The strong interaction between Fe and Si is the cause of the high stability of the Si doped θ-Al$_{13}$Fe$_4$ crystals at ambient conditions.

The primary Fe-IMCs form at elevated temperature, typically between 600 °C and 800 °C during casting processes [1-3, 11, 12]. At such high temperature, extra freedom of due to partial Si occupation at the Al sites becomes an important factor in determination of relative stability of the configurations. Here we estimate the contribution of configurational entropy to the relative stability of the Si doped structures at elevated temperature.

The Gibbs energy of a system is defined as $\Delta G = \Delta H - T \Delta S_{\text{config}}$, here ΔH is the change of enthalpy, and T is the temperature, when we only discuss the effect of number of configurations of systems. The change of configuration entropy is defined as, $\Delta S_{\text{config}} = R \ln W$, R is the Boltzmann constant, W the number of configurations. Table S-II includes the numbers of configurations (W) for the Si doped θ-Al$_{13}$Fe$_4$ crystals. Using the data listed in Table S-II, we calculated the configurational entropies to the relative stability of the Si doped θ-Al$_{13}$Fe$_4$ crystals at 1000 K. The results are included in Table S-II and plotted in Fig. 2.

The contribution of configurational entropy has influences on the relative stability of the crystal of different Si contents at high temperature. The most stable ones at 1000 K are: Al$_{73}$Si$^{\text{IX}}_3$ Si$^{\text{VIII}}_2$Fe$_{24}$ (ΔG = -0.392 eV) with $x = 0.0641$; Al$_{75}$Si$^{\text{IX}}_2$ Si$^{\text{VIII}}_1$Fe$_{24}$ (ΔG = -0.382 eV) with $x = 0.0385$ in the formula (Al$_{1-x}$Si$_x$)$_{13}$Fe$_4$, as well as the structure with 3Si at Al9 and 1Si at Al8, Al$_{74}$Si$^{\text{IX}}_3$Si$^{\text{VIII}}_1$Fe$_{24}$ (ΔG = -0.368 eV) ($x = 0.0513$) (Fig. 2). These configurations are different from the case at 0 K where Al$_{74}$Si$^{\text{IX}}_4$Fe$_{24}$ is the most stable as shown in Fig. 2. However, the general trend of the relative stability of the Si doped θ-Al$_{13}$Fe$_4$ crystals on Si is unchanged. The maximum of Si doping composition is still the same. The Gibbs energy remains positive even we include the contribution of configurational entropy for the crystal contains 4Si at Al9, 3Si at Al8 and 3Si at Al6. This case has a large number of configurations W = 64 (Table S-II).

The analysis also indicates that the chemical potential of an alloy has also impact on the formation of θ-(Si,Al)$_{13}$Fe$_4$ crystals in Al-alloy melt under different casting conditions. Under the conditions the Si content is relatively low and the cooling rate is relatively high, and the Si content in solidified θ-(Al,Si)$_{13}$Fe$_4$ crystals is expected to be low with dominating Al$_{75}$Si$^{\text{IX}}_2$Si$^{\text{VIII}}_1$Fe$_{24}$ component, whereas under the conditions of high Si content and quick cooling one expects dominating Al$_{73}$Si$^{\text{IX}}_3$Si$^{\text{VIII}}_2$Fe$_{24}$ component. Correspondingly, slow cooling rate enhances solidified θ-(Al,Si)$_{13}$Fe$_4$ crystals with Al$_{74}$Si$^{\text{IX}}_4$Fe$_{24}$ dominance.

The ternary Al-Fe-Si phase diagrams showed that between 600 °C to 1000 °C, the maximum Si content in θ-Al$_{13}$Fe$_4$ is about 2 at.% to 3 at.% [15-18], which corresponds to (Al$_{1-x}$Si$_x$)$_{13}$Fe$_4$ with $x = 0.026$ to 0.039, respectively. Recently, Que obtained single crystals for both pure θ-Al$_{13}$Fe$_4$ and θ-(Al$_{1-x}$Si$_x$)$_{13}$Fe$_4$ with x = 0.026 in the cast Al alloys [3, 37]. The experimental values are overall in line with our analysis that for θ-(Al$_{1-x}$Si$_x$)$_{13}$Fe$_4$, the x value is between 0.038 to 0.064 with consideration of the chemical compositions and experimental conditions.

In brief, the present first-principles study revealed Si solution on theAl9 and Al8 sites in θ-Al$_{13}$Fe$_4$ at ambient conditions. The lattice parameters of unit cell decrease with Si content in a linear way. The calculated results are in good agreement with the experiments available in the literature and recent experimental measurements [3, 37]. The obtained information helps us to get insight into the formation regions of the θ-(Al,Si)$_{13}$Fe$_4$ phase at various conditions. Moreover, the present approach can be applied to the other Fe-IMCs to get a comprehensive understanding of the phase relations in the Al-Fe-Si ternary system and the formation of Fe-IMCs in casting processes of Al alloys.

4. Conclusions

A first-principles DFT approach has been applied to study the formation, stability and structural properties of Si doping in the Al-rich intermetallic compound, θ-Al$_{13}$Fe$_4$. Clearly Si atoms prefer solution on the Al9 and Al8 sites, whereas Si replacement of Fe in θ-Al$_{13}$Fe$_4$ is unlikely. The chemical composition with the lowest formation energy is Al$_{74}$Si$^{IX}_4$Fe$_{24}$ and the composition with highest Si content corresponds to Al$_{70}$Si$^{IX}_4$Si$^{VIII}_4$Fe$_{24}$ (the Roman numerals represent the Al sites), respectively. The doped Si atoms have strong covalent interaction with neighbouring Fe atoms. The Si doped θ-Al$_{13}$Fe$_4$ crystals exhibit ionic, covalent and metallic triple nature. The lattice parameters and volume of the unit cell of the Si doped θ-Al$_{13}$Fe$_4$ crystals decrease with increasing Si content in a linear manner. The calculated results are overall agree with the available experimental observations. The origin of Si doping in θ-Al$_{13}$Fe$_4$ stems from the strong Si-Fe chemical bonding and repulsive interaction between Si and Al. The obtained information about Si incorporation in θ-Al$_{13}$Fe$_4$ is helpful to understand the thermal equilibria of Al(Si)-Fe systems, and further to have a comprehensive understanding about formation of and competence among the Fe-IMCs under the casting conditions for Al-based alloys.

Acknowledgements

Declaration of interests

None.

References

1)   L. F. Mondolfo, Aluminum Alloys: Structure and properties, Butterworths, London (1976).

2)   L. F. Zhang, J. W. Gao, L. Nana, W. Damoah and D. G. Robertson, Removal of iron aluminum: A review, Mineral Processing & Extractive Metall. Rev. 33 (2012) 99-157.

3)   Z. P. Que, Y. Wang and Z. Fan, Formation of the Fe-containing intermetallic compounds during solidification of Al-5Mg-2Si-0.7Mn-1.1Fe alloy, Metal. Mater. Trans. A49 (2018) 2173-2181.

4)   M. E. Schlesinger, Aluminum recycling, Taylor & Francis group, Milton Park, Abingdon-on-Thames, Oxfordshire 2017.

5)   A. Gesing, L. Berry, R. Dalton and R. Wolanski, Assuring continued recyclability of automotive aluminum alloys: grouping of wrought alloys by color, X-ray adsorption and chemical composition-based sorting, TMS 2002 Annual Meeting: Automotive Alloys and Aluminum Sheet and Plate Rolling and Finishing Technology Symposia, Seattle, WA: Minerals, Metals and Materials Society (TMS) (2002) p3-17.

6)   B. Sundman, I. Ohnuma, N. Dupin, U. R. Kattner and S. G. Fries, An assessment of the entire Al-Fe system including D0(3) ordering, Acta Mater. 57 (2009) 3896-2908.

7)   T. Zienert and O. Fabrichnaya, Experimental investigation and thermodynamic assessment of the Al-Fe system, J. Alloys Compd. 743 (2018) 795-811.

8)   X. L. Li, A. Scherf, M. Heilmaier and F. Stein, The Al-rich part of the Fe-Al phase diagram, JPEDAV 37 (2016) 162-173.

9)   S. G. Shabestari, The effect of iron and manganese on the formation of intermetallic compounds in aluminum-silicon alloys, Mater. Sci. Eng. A383 (2004) 289-298.

10)   D. V. Malakhov, D. Panahi and M. Gallernault, On the formation of metallics in rapidly solidifying Al-Fe-Si alloys, CALPHAD 34 (2010) 159-166.

11)   J. A. Taylor, Iron-containing intermetallic phases in Al-Si based casting alloys, Procedia Materials Science 1 (2012) 19-33.

12)   C. M. Allen, K. A. Q. O'Reilly, B. Cantor and P. V. Evans, Intermetallic phase selection in 1XXX Al alloys, Prog. Mater. Sci. 43 (1998) 89-170.

13)   J. Grin, U. Burkhard, M. Ellner and K. Peters, Refinement of the Fe_4Al_{13} structure and its relationship to the quasihomogical homeotypical structures, Z. Kristal. 209 (1994) 479-487.

14)   W. Khalifa, F. H. Samuel and J. E. Gruzleski, Iron intermetallic phases in the Al corner of the Al-Si-Fe system, Metall. Mater. Trans. A34 (2003) 807-825.

15)   N. Krendelsberger, F. Weitzer and J. C. Schuster, On the reaction scheme and liquidus surface in the ternary system Al-Fe-Si, Metall. Mater. Trans. A38 (2007) 1681-1691.

16)   G. Ghosh, *Aluminium – Iron – Silicon*, in SpringerMaterials, G. Effenberg and S. Ilyenko (ed.) Landolt-Börnstein – Group IV physical Chemistry 11D1 (iron Sytems, Part) 2008.

17)   M. C. J. Marker, B. Skolyszewska-Kühberger, H. S. Effenberger, C. Schmetterer and K. W. Richter, Phase equilibria and structural investigations in the system Al-Fe-Si, Intermetallics, 19 (2011) 1919-1929.

18)   V. Stefániay, A. Griger and T. Turmezey, Intermetallic phases in the aluminium-side corner or the AlFeSi-alloy system, J. Mater. Sci. 22 (1987) 539-546.

19)   P. Popčević, A. Smontara, J. Ivkov, M. Wencka, M. Komelj, P. Jeglič, S. Vrtnik, M. Bohnar, Z. Jagličić, B. Baer, P. Gille, H. Borrmann, U. Burkhardt, Yu. Grin and J. Dolinšek, Anisotropic physical properties of the $Al_{13}Fe_4$ complex intermetallic and its ternary derivative $Al_{13}(Fe, Ni)_4$, Phys. Rev. B81 (2010) 184203.

20)   P. Jeglič, S. Vrtnik, M. Bobnar, M. Klanjšek, B. Bauer, P. Gille, Yu. Grin, F. Haarmann and J. Dolinšek, M-Al-M groups trapped in cages of $Al_{13}M_4$ (M = Co, Fe, Ni, Ru) complex intermetallic phases as seen via NMR, Phys. Rev. B82 (2010) 104201.

21)   T. Zienert, A. Leineeber and O. Fabrichnaya, Heat capacity of Fe-Al intermetallics: B2-FeAl, $FeAl_2$, Fe_2Al_5 and Fe_4Al_{13}, J. Alloys and Compounds 725 (2017) 848-859.

22)   A. van Alboom, B. Lemmens, B. Breitbach, E. de Grave, S. Cottenier and K. Verbeken, Multi-method identification and characterization of the intermetallic surface layers of Al-coated steel: $FeAl_3$ or Fe_4Al_{13} and Fe_2Al_5 or Fe_2Al_{5+x}, Surface & Coating Technology 324 (2017) 419-428.

23)   J. Ledieu, È. Gaudry, L. N. Loli, S. A. Villaseca, M. C. de Weerd, M. Hahne, P. Gille, J. M. Dubois and V. Fournée, Structural investigation of the (010) surface of the $Al_{13}Fe_4$ catalyst, Phys. Rev. Lett. 110 (2013) 076102.

24)   M. Armbrüster, K. Kovnir, M. Friedrich, D. Teschner, G. Wowsnick, M. Hahne, P. Gille, L. Szentmiklósi, M. Feuerbacher, M. Heggen, F. Girgsdies, D. Rosenthal, R. Schlögl and Yu. Grun, $Al_{13}Fe_4$ as a low-cost alternative for palladium in heterogeneous hydrogenation, Nature Materials 11 (2012) 690-693.

25)   C. M. Fang, A. Dinsdale, Z.P. Que and Z. Fan, Intrinsic defects in and electronic properties of θ-$Al_{13}Fe_4$: An ab initio DFT study, J. Phys.: Materials 2 (2019)015004.

26)   A. Dinsdale, C. M. Fang, Z. P. Que and Z. Fan, Understanding the thermodynamics and crystal structure of complex Fe containing intermetallic phases formed on solidification of aluminium alloys, JOM 71 (2019) 1731-1736.

27)   G. Kresse, J. Hafner, *Ab initio* molecular-dynamics simulation of the liquid-metal-amorphous-semiconductor transition in germanium, Phys. Rev. B49 (1994) 14251-14269.

28)   G. Kresse, J. Furthmüller, Efficiency of *ab-initio* total energy calculations for metals and semiconductors using a plane-wave basis set, Comp. Mater. Sci. 6 (1996) 15-50.

29)   P. E. Blöchl, Projector augmented-wave method, Phys. Rev. B50 (1994) 17953-17978.

30)   G. Kresse, J. Joubert, From ultrasoft pseudopotentials to the projector augmented-wave method, Phys. Rev. B59 (1999) 1758-1775.

31)   J. P. Perdew, K. Burke, M. Ernzerhof, Generalized gradient approximation made simple, Phys. Rev. Lett. 77 (1996) 3865-3868.

32)   C. M. Fang, M. H. F. Sluiter, M. A. van Huis, C. K. Ande and H. W. Zandbergen, Origin of predominance of cementite among iron carbides in steel at elevated temperature, Phys. Rev. Lett. 105 (2010) 055503.

33)   H. J. Monkhorst, J. D. Pack, Special points for Brillouin-zone integrations, Phys. Rev. B13 (1976) 5188-5192.

34)   R. W. G. Wyckoff, The structure of Crystals, Reinhold Publishing Corporation, New York 1935.

35)   J. Arblaster, Selected values of the crystallographic properties of the elements, ASM International, Materials Park, Ohio 2018.

36)   W. Zheng, S. He, M. Selleby Y. He, L. Li X.-G. Lu and J. Ågren, Thermodynamic assessment of the Al-C-Fe system, CALPHAD 58 (2017) 34-49.

37)   Z. P. Que, unpublished results.

38)   E. Torun, C. M. Fang, G. A. de Wijs, and R. A. de Groot, Role of magnetism in catalysis RuO_2(110) surface, J. Phys. Chem. C117 (013) 6353-6357.

39)   R.F.W. Bader, A bond path: A universe indicator of bonded interactions, J. Phys. Chem. A102 (1998) 7314-7323.

40)   G. Henkelman, A. Arnaldsson, H. Jónsson, A fast and robust algorithm for Bader decomposition of charge density, Comput. Mater. Sci. 36 (2006) 354-360.